Digest Journal of Nanomaterials and Biostructures

Dig. J. Nanomater. Bios. **2026**; 21(4): 62021
https://doi.org/10.31083/DJNB62021

Original Research

Calcium-Controlled Tuning of $Zn_{0.25}Co_{0.5}Ca_{0.25}Fe_{1.97}Ba_{0.03-y}Ca_yO_4$ Ferrites for MHz-Range Electromagnetic Interference Shielding in Biomedical Electronic Systems

Muhammad Imran Arshad[1], Maria Akhtar[1,2], Zeshan Munir[1], Al-Badrawy Abo El-Nasr[3], M. Ajaz-un-Nabi[1], Nasir Amin[1], Hafiz Tauqeer Ali[3], Kiran Mehmood[1], Uswa Mubarik[1,*]

[1]Magnetic Interfaces & Materials Innovation (MiMi) Nanotech Research Lab, Department of Physics, Government College University, 38000 Faisalabad, Pakistan
[2]Center for High Energy Physics, University of The Punjab, 54000 Lahore, Pakistan
[3]Department of Mechanical Engineering, College of Engineering, Taif University, 21944 Taif, Saudi Arabia
*Correspondence: uswamubarik2301@gmail.com (Uswa Mubarik)
Academic Editor: Shaik Gouse Peera
Submitted: 4 January 2026 Revised: 9 July 2026 Accepted: 24 July 2026 Published: 3 November 2026

Abstract

Background: Spinel ferrites are widely used for electromagnetic interference (EMI) shielding in biomedical devices and high-frequency electronics because of their tunable structural, magnetic, and dielectric properties. However, the effect of progressive Ca^{2+} substitution on the properties of $Zn_{0.25}Co_{0.5}Ca_{0.25}Fe_{1.97}Ba_{0.03-y}Ca_yO_4$ ferrites has not been systematically investigated. **Methods:** $Zn_{0.25}Co_{0.5}Ca_{0.25}Fe_{1.97}Ba_{0.03-y}Ca_yO_4$ (y = 0.00, 0.01, 0.02, 0.03) nanoparticles were synthesized using a sol–gel autocombustion method, and their structural, vibrational, magnetic, electrical, and dielectric properties were characterized using X-ray diffraction (XRD) with Rietveld refinement, Raman spectroscopy, vibrating sample magnetometry (VSM), temperature-dependent current–voltage measurements, and dielectric spectroscopy (4Hz–8 MHz). **Results:** XRD with Rietveld refinement revealed a predominantly single-phase cubic spinel structure with crystallite sizes of 15.10–18.06 nm and trace α-Fe_2O_3. Raman spectra revealed five characteristic modes, while peak shifts and A_{1g} subband splitting indicated Fe^{2+}/Fe^{3+} redistribution and increased inversion. The y = 0.02 sample exhibited the highest saturation magnetization (72.73 emu/g), coercivity (746.92 Oe), anisotropy constant (56,587 erg/cm^3), and resonance frequency (16.06 GHz), whereas the y = 0.01 sample showed the highest alternating-current conductance. All samples showed semiconducting behavior and non-Debye dielectric relaxation. **Conclusions:** Controlled Ba^{2+}/Ca^{2+} substitution effectively tailors the structural, magnetic, electrical, and dielectric properties of Zn–Co spinel ferrites. The y = 0.02 composition demonstrates the best overall performance and is therefore a promising candidate for MHz-range EMI shielding and biomedical electronic applications.

Keywords: sol-gel auto combustion method; calcium substitution; dielectric properties; electrical resistivity; bio-medical electronic devices

1. Introduction

The design and development of ferrite materials have garnered significant interest due to the increasing demand for efficient, high-performance materials in advanced technological applications. Among these, spinel ferrites have gained significant interest due to their distinctive combination of dielectric, magnetic, and electrical properties. Owing to these characteristics, they serve as essential components in energy storage systems, transformers, inductors, antennas, and high-frequency devices [1]. The spinel structure, with a general formula AB_2O_4, is inherently flexible and provides a stable framework for modifying electrical and magnetic characteristics to specific applications by allowing a wide range of cation substitutions at the tetrahedral (A) and octahedral (B) lattice sites. Among these spinel ferrites, cobalt ferrite ($CoFe_2O_4$) and its doped variants are particularly attractive due to their high magneto-crystalline anisotropy, moderate saturation magnetization, and large coercivity [2]. Ionic substitution effectively modifies the dielectric properties of cobalt ferrites, thereby enhancing their functionality in applications such as electromagnetic wave absorbers, inductors, gas sensors, biomedicine, and multiferroic devices [3,4,5,6]. The substitution of non-magnetic ions such as Zn^{2+}, Ca^{2+}, or Ba^{2+} in place of Co^2 significantly influences conduction mechanisms, dielectric relaxation, and polarization behavior [7]. Similarly, Ca^{2+} ions, owing to their large ionic radius and non-magnetic nature, induce lattice strain and alter the concentration of oxygen vacancies, which play a crucial role in regulating frequency dispersion and dielectric loss [8].

The incorporation of Ba^{2+} into spinel ferrites shows significant promise for dielectric optimization, although it has been less extensively studied. Due to their much larger ionic radius (1.61 Å) compared to Co^{2+} (0.74 Å) and Zn^{2+}

Copyright: © 2026 The Author(s). Published by IMR Press.
This is an open access article under the CC BY 4.0 license.

Publisher's Note: IMR Press stays neutral with regard to jurisdictional claims in published maps and institutional affiliations.

(0.74 Å), Ba^{2+} ions are likely to occupy interstitial positions or segregate at grain boundaries, thereby promoting densification and modifying the dielectric response through space charge polarization. Furthermore, they do not readily fit into the conventional spinel lattice [9]. Moreover, by creating oxygen vacancies or Fe^{2+} ions and changing the material's conduction routes, Ba doping may facilitate charge compensation [10].

In addition to conventional electronic and communication systems, electromagnetic interference (EMI) has emerged as a critical concern in the biomedical environment, where sensitive diagnostic instruments, implantable devices, and wearable healthcare electronics operate predominantly in the MHz frequency range. Uncontrolled electromagnetic radiation can lead to signal distortion, malfunction, or degradation in the performance of medical equipment.

Recent advances in nanoscale synthesis methods, particularly sol-gel, hydrothermal, and citrate-nitrate autocombustion techniques, have enabled precise control over cation stoichiometry and microstructure, both of which are critical for tailoring the dielectric properties of substituted ferrites. These methods offer advantages such as atomic-scale homogeneous mixing, low processing temperatures, and the formation of highly crystalline nanophases, which enhance the electrical and dielectric properties of the material [11].

In this study, we report the synthesis and comprehensive dielectric analysis of a novel multicomponent spinel ferrite system, $Zn_{0.25}Co_{0.5}Ca_{0.25}Fe_{1.97}Ba_{0.03-y}Ca_yO_4$, (y = 0, 0.01, 0.02, and 0.03). This composition was designed based on a co-doping strategy aimed at enhancing dielectric performance through the synergistic effects of Zn^{2+}, Ca^{2+}, and Ba^{2+} ions. Ba^{2+} is expected to influence space charge polarization and grain boundary conduction, whereas Zn^{2+} and Ca^{2+} affect cation distribution of A- and B-sites as well as electronic hopping efficiency. The gradual substitution of Ba^{2+} with Ca^{2+} enables the investigation of compositional tuning on phase purity and dielectric properties. The synthesized samples were characterized using Current-Voltage analysis (I-V), vibrating sample magnetometry (VSM), Raman spectroscopy, and dielectric measurements to evaluate the relationship between structural modifications and the resulting functional behavior. The findings of this study provide new insight into the impact of selective cation substitution on the performance of spinel ferrite materials.

2. Experimental Section

2.1 Materials and Methods

The nanoparticles of $Zn_{0.25}Co_{0.5}Ca_{0.25}Fe_{1.97}Ba_{0.03-y}Ca_yO_4$ (y = 0, 0.01, 0.02, 0.03) were synthesized via the sol-gel auto combustion route. The reagents used were zinc nitrate ($Zn(NO_3)_2{\cdot}4H_2O$), cobalt nitrate ($Co(NO_3)_26H_2O$), calcium nitrate ($Ca(NO_3)_2{\cdot}4H_2O$), iron nitrate ($Fe(NO_3)_3{\cdot}9H_2O$), barium nitrate ($Ba(NO_3)_2{\cdot}4H_2O$) to synthesize calcium doped ferrites. The chemicals were dissolved in distilled water and then subjected to bath sonication to make a homogenous mixture. The citric acid was added in a molar ratio of 1:1. The solution mixture was placed on a magnetic stirrer. With the continuous stirring, ammonia was added dropwise to maintain the solution pH at 7. By heating the solution at 80 ℃, sol was formed, which then converted into a transparent gel. By further heating at 350 ℃, this viscous gel was burnt, and fluffy ash-like powder was obtained. The resulting powder was then ground and sintered at 850 °C for 8 h. Fig. 1 represents the whole process.

2.2 Characterization Tools

The crystal structure of the synthesized samples was examined by X-ray diffraction (XRD) using a D8 ADVANCE diffractometer (Bruker Corporation, Karlsruhe, Germany) with Cu Kα radiation (λ = 1.5406 Å). Raman spectroscopy was performed using a MINSTEX PRI100 Raman spectroscopy system (DONGWOO, Gwangju, South Korea) to investigate the vibrational modes of the synthesized ferrite samples. Room-temperature magnetic behavior of the powdered samples was assessed using a Vibrating Sample Magnetometer (VSM Model 175, Princeton Applied Research (PAR), Princeton, NJ, USA). Direct current (DC) electrical resistivity was measured with a two-probe I–V setup (Keithley Model 2401, Keithley Instruments, Cleveland, OH, USA), while dielectric properties were evaluated using an Inductance, Capacitance, and Resistance (LCR) meter (HIOKI IM-3536, E.E. Corporation, Nagano, Japan) over a frequency range of 4 Hz to 8 MHz.

3. Results

3.1 XRD Analysis

Fig. 2 shows the X-ray diffraction patterns of $Zn_{0.25}Co_{0.5}Ca_{0.25}Fe_{1.97}Ba_{0.03-y}Ca_yO_4$ ferrites (y = 0.00, 0.01, and 0.02). The diffraction peaks at 2θ = 30.1°, 35.3°, 43.1°, and 57.0° were identified as (220), (311), (400), and (511) crystallographic planes, respectively, establishing the cubic spinel ferrite structure [12]. The (311) peak shows the highest intensity, indicating the most preferred growth direction of synthesized ferrite nanoparticles.

The characteristic spinel reflections are also seen in the patterns, together with a few weak diffraction peaks indicated by (*). These peaks were correlated to a small amount of α-Fe_2O_3 (hematite) secondary phase [13]. The presence of these lower-intensity hematite reflections might be related to small amounts of iron segregation during the calcination. Nevertheless, the synthetic samples are predominantly single-phase spinel ferrites, as the amount of secondary phase is very small because of their very low intensity. With the increasing of Ca^{2+} concentration, the peak positions shift slightly and the peak intensities vary, which

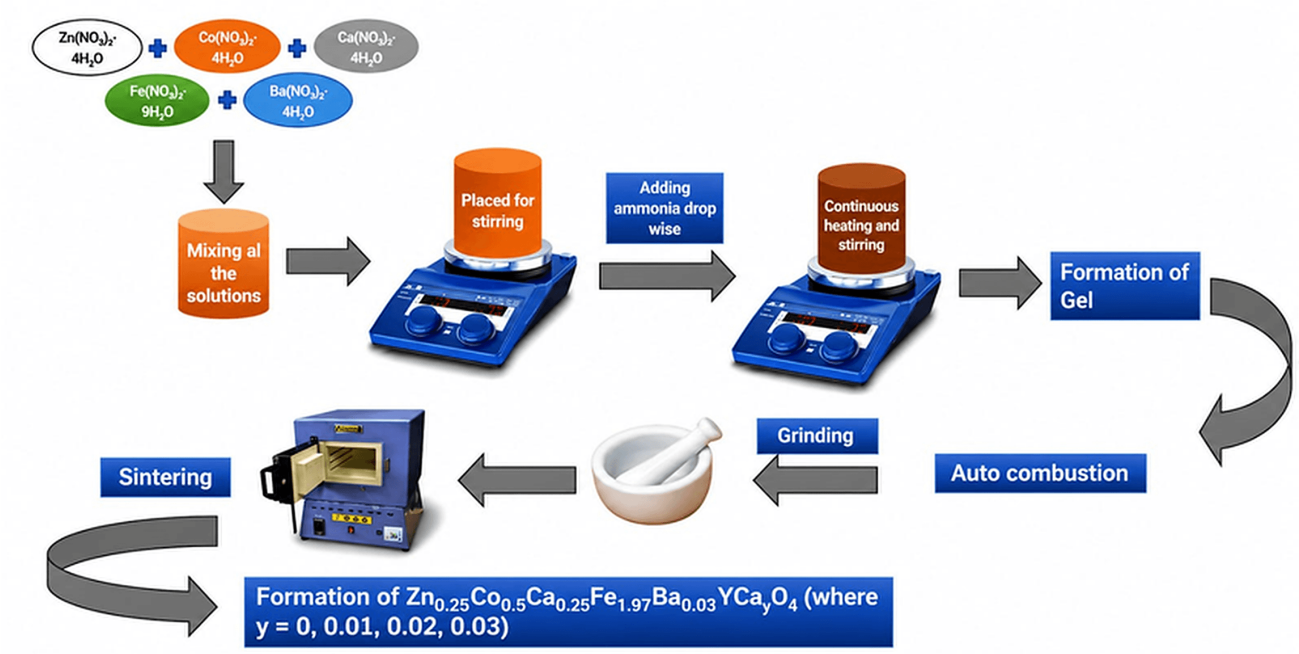


Fig. 1. Synthesis of $Zn_{0.25}Co_{0.5}Ca_{0.25}Fe_{1.97}Ba_{0.03-y}Ca_yO_4$.

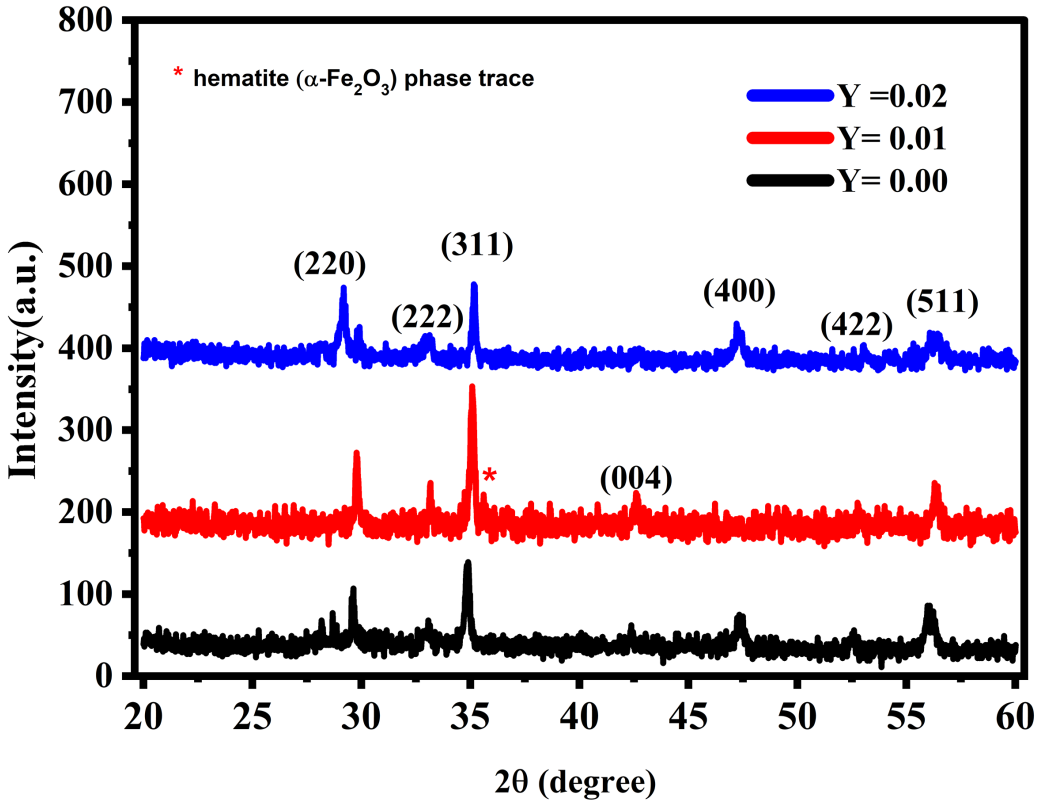


Fig. 2. XRD peaks of $Zn_{0.25}Co_{0.5}Ca_{0.25}Fe_{1.97}Ba_{0.03-y}Ca_yO_4$. XRD, X-ray diffraction.

suggests successful incorporation of the Ca^{2+} ions into the lattice of the ferrite. The ionic radii of Ca^{2+} are not the same as those of the substituted ions, so that lattice distortions and changes in the interplanar spacing are produced upon incorporation. Furthermore, a slight peak width broadening was noticed in Ca substitution, indicating the changes in crystallite size and lattice strain. The crystallite size (D) was estimated from the most intense (311) diffraction peak using the Debye–Scherrer equation [14]:

Table 1. XRD parameters of $Zn_{0.25}Co_{0.5}Ca_{0.25}Fe_{1.97}Ba_{0.03-y}Ca_yO_4$.

Parameters	(hkl)	2θ (degree)	FWHM (degree)	d-spacing (Å)	Lattice constant (Å)	Crystallite size (nm)	R_{wp}	R_{exp}	χ^2
y = 0.00	311	35.2	0.50	2.55	8.46	16.61	48.52	39.44	1.23
y = 0.01	311	35.0	0.46	2.56	8.49	18.06	53.76	40.42	1.33
y = 0.02	311	35.4	0.55	2.53	8.39	15.10	42.37	37.83	1.12

FWHM, full width at half maximum.

$$D = \frac{k\lambda}{\beta \cos\theta} \quad (1)$$

Here, k is the shape factor (0.9), λ is the wavelength of Cu-Kα radiation (1.5406 Å), β is the full width at half maximum (FWHM), and θ is the Bragg diffraction angle. The calculated crystallite size is found to lie in the range of 15.10–18.06 nm, indicating the nanocrystalline nature of the synthesized ferrites. The crystallite size of the sample with y = 0.01 is the largest (18.06 nm), while the y = 0.02 composition is the smallest (15.10 nm). The non-monotonic variation in crystallite size with increasing Ca concentration is believed to be due to the lattice strain and defects created by the substitution of Ca, which in turn inhibits grain growth at higher doping levels.

The lattice constant shows a small variation with the increase in Ca content, which further strengthens the evidence that the incorporation of Ca^{2+} ions into the spinel lattice was successful and that the lattice experienced distortion. These results are summarized in Table 1.

Fig. 3a–c shows the Rietveld refinement of the XRD patterns for all $Zn_{0.25}Co_{0.5}Ca_{0.25}Fe_{1.97}Ba_{0.03-y}Ca_yO_4$ compositions, confirming the single-phase cubic spinel structure. The close agreement between experimental and calculated profiles, evidenced by flat difference curves and low residual values, validates the structural model. All observed reflections (220), (311), (222), (400), (422), (511), and (440) are consistent with the spinel phase. The systematic variation in peak positions with Ca^{2+} content reflects the progressive change in lattice parameter, attributed to the substitution of the smaller Ca^{2+} ion at the Ba^{2+} site.

3.2 Raman Spectroscopy

Fig. 4 shows the Raman spectra of the prepared samples at room temperature for different compositions (y = 0.00 to 0.03), within the 200–950 cm^{-1} range. The spectra exhibit several characteristic vibrational modes that confirm the crystal structure of the material [15]. The intensities of Raman modes increase with increasing Ca substitution (y). The incorporation of Ca^{2+} ions enhances long-range ordering. Additionally, slight shifts in peak positions are observed, suggesting local structural distortions in the lattice [16].

Five distinct Raman-active modes were observed in all compositions. These modes correspond to T_2g (1), Eg, T_2g (2), T_2g (3) and A_1g modes as depicted in Table 2. The clear presence of these modes confirms the retention of a highly ordered crystalline phase across the entire compositional range [15]. The T_2g (1) and A_1g modes are observed in the ranges of 325.44–328.74 cm^{-1} and 696.6–706.65 cm^{-1}, respectively, and are associated with the metal ion vibrations at tetrahedral (A) sites. The shift in the T_2g (1) mode, with increasing Ca concentrations (y = 0.00 to 0.03), suggests a slight bond shortening within the tetrahedral sublattice. The A_1g peak exhibits a downshift from 706.65 cm^{-1} to 696.69 cm^{-1}, indicating the elongation of metal–oxygen bonds at the A site, due to Ca^{2+} substitution [17]. The E_g mode, associated with the symmetric bending vibration of oxygen atoms at the octahedral (B) sites, exhibits a significant non-monotonic trend. The E_g mode initially shifts from 406.70 cm^{-1} (y = 0.00) to 476.27 cm^{-1} (y = 0.01), then decreases sharply to 373.42 cm^{-1} (y = 0.02), and finally recovers slightly to 378.85 cm^{-1} (y = 0.03). This complex shift suggests that local ionic rearrangement and changes in metal–oxygen bond strengths with Ca content significantly altered the octahedral site environment [18]. With increasing Ca substitution, the T_2g (2) and T_2g (3) modes located in the ranges of 478.03–479.57 cm^{-1} and 544.51–551.81 cm^{-1}, respectively, exhibit modest but consistent upward shifts [19].

Table 2. Raman modes of $Zn_{0.25}Co_{0.5}Ca_{0.25}Fe_{1.97}Ba_{0.03-y}Ca_yO_4$.

Y	Raman Shift (cm^{-1})				
	T_2g (1)	Eg	T_2g (2)	T_2g (3)	A_1g
	Tetrahedral (A) Site	Octahedral (B) Site			Tetrahedral (A) Site
0.00	325.44	406.70	478.03	544.51	706.65
0.01	328.74	476.27	479.57	550.53	703.11
0.02	327.9	373.42	478.86	547.85	697.88
0.03	328.33	378.85	479.41	551.81	696.69

Peak deconvolution in Fig. 5a–d reveals the sub-band structure of each vibrational mode and provides direct evidence of progressive cation redistribution. In the undoped composition, two balanced A_1g sub-components confirm an ordered Fe^{2+}/Fe^{3+} distribution at the tetrahedral site. Upon Ca^{2+} introduction (y = 0.01), the higher-wavenumber A_1g component intensifies, consistent with preferential Fe^{2+}/Fe^{3+} oxidation for charge compensation.

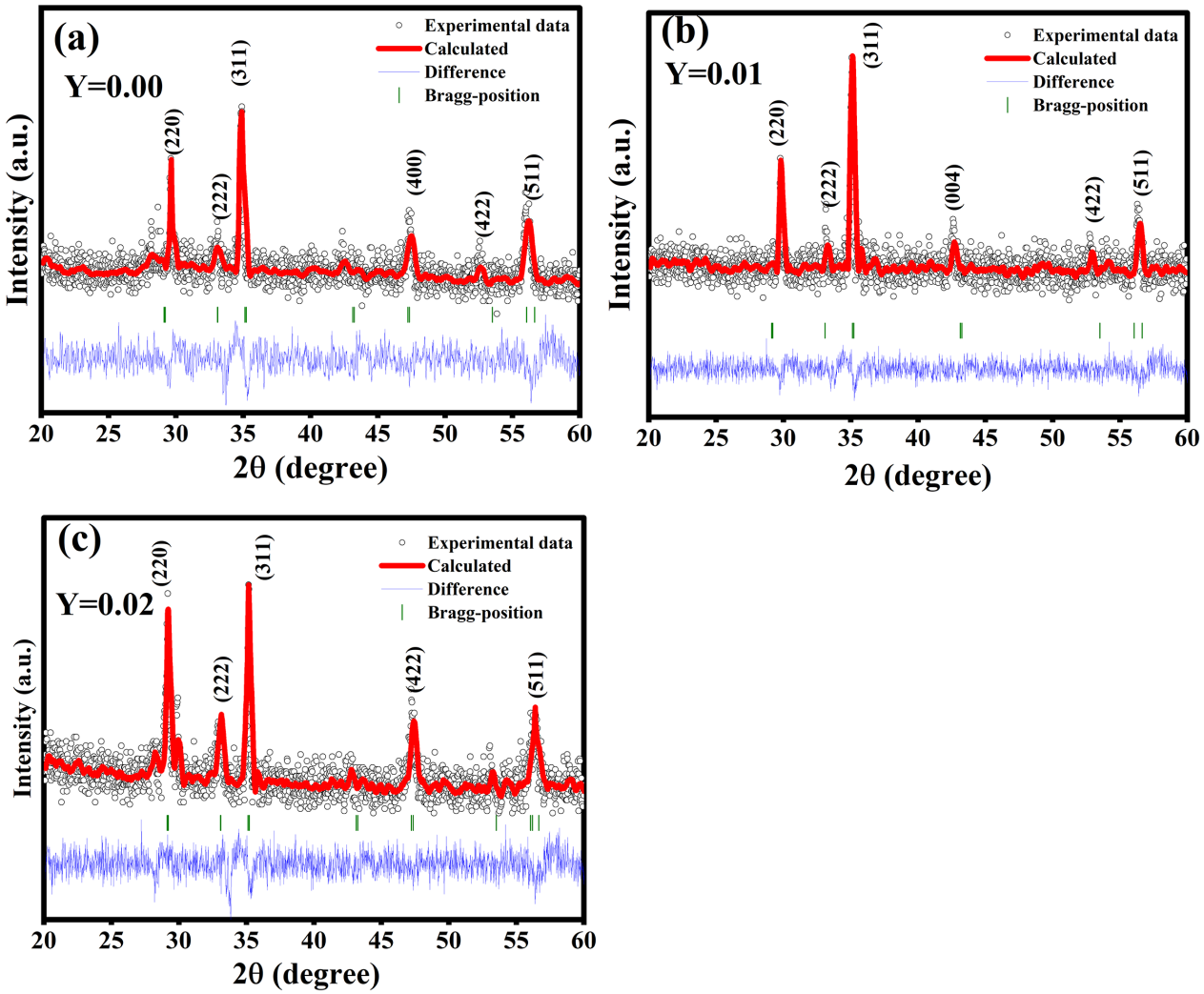


Fig. 3. Rietveld refinement plots of $Zn_{0.25}Co_{0.5}Ca_{0.25}Fe_{1.97}Ba_{0.03-y}Ca_yO_4$. (a) y = 0.00, (b) y = 0.01, and (c) y = 0.02.

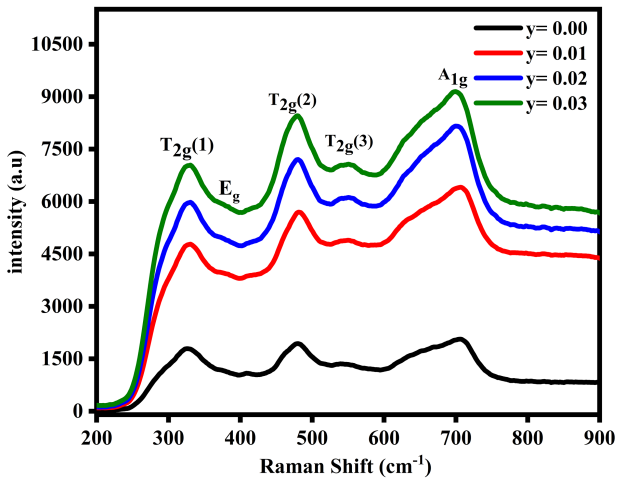


Fig. 4. Raman spectra of $Zn_{0.25}Co_{0.5}Ca_{0.25}Fe_{1.97}Ba_{0.03-y}Ca_yO_4$.

At y = 0.02, the A_1g band deconvolutes into three distinct components, indicating maximum multiplicity of local Fe-O environments and peak modification of the spinel inversion degree. A broad sub-peak emerging at 800–950 cm^{-1} as y increases is attributed to local distortion modes associated with oxygen vacancy formation. At y = 0.03, equalization of A_1g sub-component intensities and maximum mode broadening confirm peak lattice disorder and onset of structural inhomogeneity at excess Ca^{2+} concentration. Collectively, these results demonstrate that Ca^{2+} substitution systematically modifies both tetrahedral and octahedral cation environments, corroborating the dielectric and magnetic property trends observed across the series.

3.3 Hysteresis Loop Analysis

Fig. 6 represents the M-H loops of $Zn_{0.25}Co_{0.5}Ca_{0.25}Fe_{1.97}Ba_{0.03-y}Ca_yO_4$ recorded at room temperature. The magnetic parameters such as saturation magnetization (M_s), remanent magnetization (M_r), coercivity (H_c), squareness ratio (M_r/M_s), anisotropy energy (K), and microwave resonance frequency (ω_m), are depicted in Table 3, indicating prominent changes in the magnetic behavior of the material.

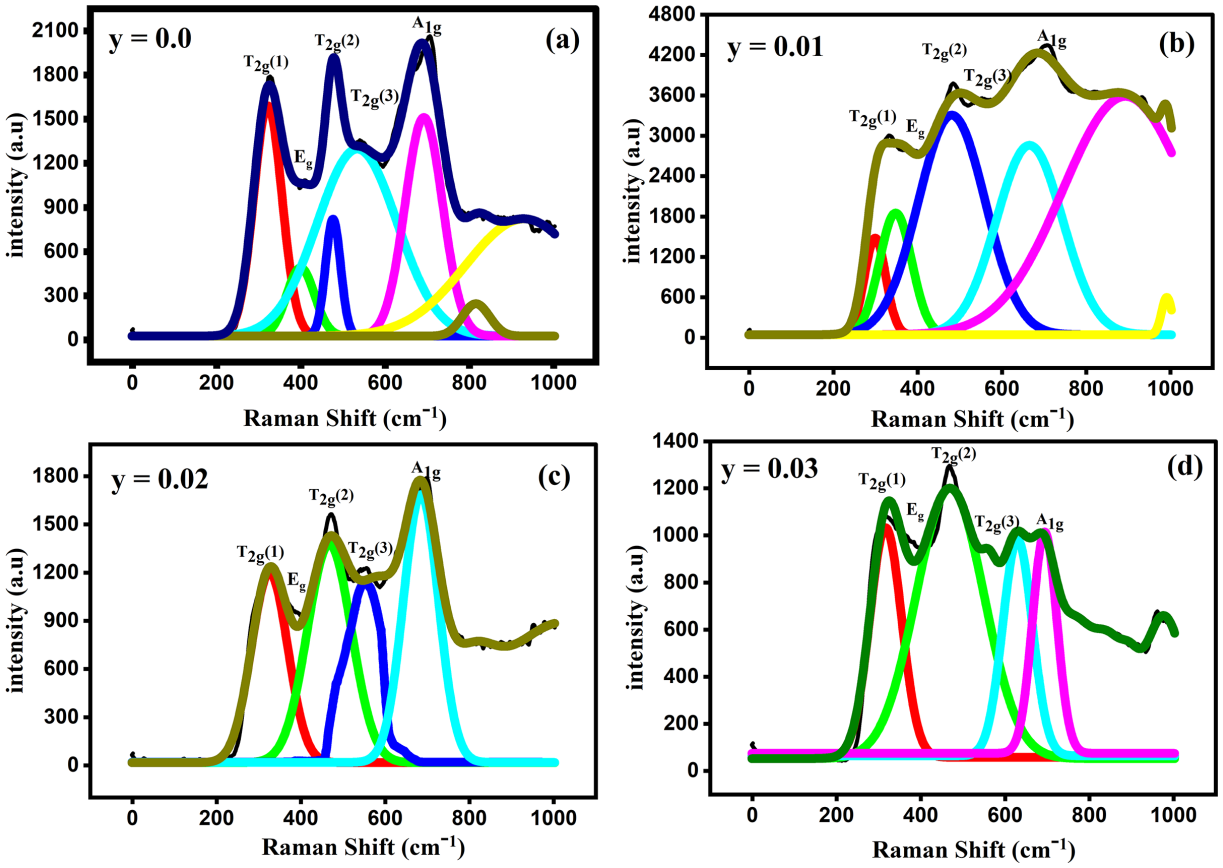


Fig. 5. Raman peak fitting of $Zn_{0.25}Co_{0.5}Ca_{0.25}Fe_{1.97}Ba_{0.03-y}Ca_yO_4$ for different values of y. (a) y = 0.00, (b) y = 0.01, (c) y = 0.02, and (d) y = 0.03.

Table 3. Magnetic parameters of $Zn_{0.25}Co_{0.5}Ca_{0.25}Fe_{1.97}Ba_{0.03-y}Ca_yO_4$.

Parameters	y = 0.00	y = 0.01	y = 0.02	y = 0.03
Ms (emu/g)	72.32	47.43	72.73	51.37
Mr (emu/g)	29.84	20.20	33.97	12.97
Hc (Oe)	640.21	561.55	746.92	374.82
Mr/Ms	0.41261	0.42589	0.46707	0.25248
K (erg/cm^3)	48229.15333	27744.07968	56586.97042	20056.77438
ω_m (GHz)	15.97224	12.93990	16.06279	11.34532

The saturation magnetization represents the maximum amount of magnetization that a material can achieve, while the remanent magnetization represents the remaining magnetization retained after the removal of the external magnetic field [20,21]. With Ca substitution, the saturation magnetization (M_s) shows a non-monotonic trend. The sample with Ca concentration y = 0.02 exhibits the highest M_s value (72.73 emu/g), which was higher than even the undoped composition (y = 0, 72.32 emu/g), this rise attributed to optimized cationic distribution and improved Fe^{3+}–O^{2-}–Fe^{3+}/Co^{2+} super exchange contacts [22]. Similar trends were seen in the remanent magnetization (M_r), which peaked at y = 0.02 (33.97 emu/g), suggesting the more successful alignment of magnetic domains in the absence of a magnetic field, associated with decreased magnetic dilution and enhanced crystallinity [23]. The resistance to demagnetization represented by the coercivity (H_c), exhibits a maximum value for the sample with y = 0.02, indicating improved magnetic stability. However, H_c significantly dropped for the sample with y = 0.03, indicating a magnetically soft nature of the composition due to magnetic dilution and increased structural disorder [24,25].

Magnetic anisotropy strongly influences the resonance frequency and coercivity. The sample with y = 0.02 shows the highest K value (56586.970), indicating its higher domain stability and coercivity. A drop in K and resonance frequency (ω_m) at y = 0.03 points to a possible reduction in high-frequency magnetic responsiveness due to a weakening of anisotropic interactions [25].

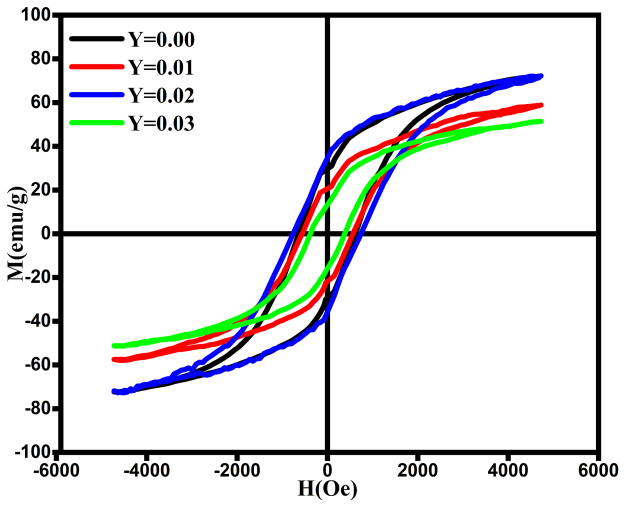


Fig. 6. Magnetization versus applied field for $Zn_{0.25}Co_{0.5}Ca_{0.25}Fe_{1.97}Ba_{0.03-y}Ca_yO_4$.

3.4 I-V Analysis

The DC resistivity of $Zn_{0.25}Co_{0.5}Ca_{0.25}Fe_{1.97}Ba_{0.03-y}Ca_yO_4$ with various Ca^{2+} ion concentrations was measured by using the probe method. The resistivity of the samples was computed by using the formula:

$$\rho = \frac{RA}{L} \tag{2}$$

where A represents the area ($A = \pi r^2$), L the thickness of circular pellets, and R is the resistance (computed as 1/slope from current voltage curves) [26]. Fig. 7 shows the temperature-dependent resistivity of as-prepared samples, by plotting the log resistivity versus 1000/K. All samples exhibit thermally activated behavior, in which resistivity decreases as temperature rises, which confirms a semiconducting nature and indicates a thermally active conduction mechanism. The conduct was consistent with the Arrhenius equation:

$$\rho = \rho_0 \exp(E_a/kT) \tag{3}$$

where ρ_0 represents the pre-exponential factor, E_a the activation energy, k represents the Boltzmann constant, and T the absolute temperature [27]. The undoped sample (y = 0.00) exhibits considerable resistivity, but upon minor substitution with Ca (y = 0.01), a significant increase in resistivity observed throughout the temperature range, due to the formation of localized states. As the Ca content rises, (y = 0.02 and y = 0.03), resistivity drops and the graphs for these two compositions overlap, indicating increased Ca doping promotes better microstructural connection between grains or enhanced hopping conduction. This trend may be associated with the Fe^{2+}/Fe^{3+} ratio, increased oxygen vacancy concentration, and better cation distribution at octahedral [28]. Therefore, the substitution of Ca^{2+} for Ba^{2+} plays a critical role in tailoring resistivity, which may have consequences for its use in electrical and magnetic devices where regulated conductivity is crucial [29].

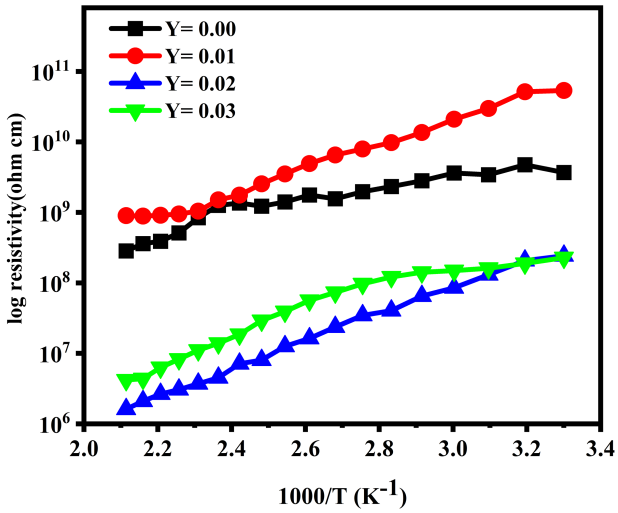


Fig. 7. Plot of 1000/T versus log of resistivity of $Zn_{0.25}Co_{0.5}Ca_{0.25}Fe_{1.97}Ba_{0.03-y}Ca_yO_4$.

Fig. 8 shows the non-linear relationship between the activation energy and the Ca content. The activation energy reaches its maximum at y = 0.02, indicating the strongest thermally activated conduction, while the highest resistivity is observed at y = 0.01.

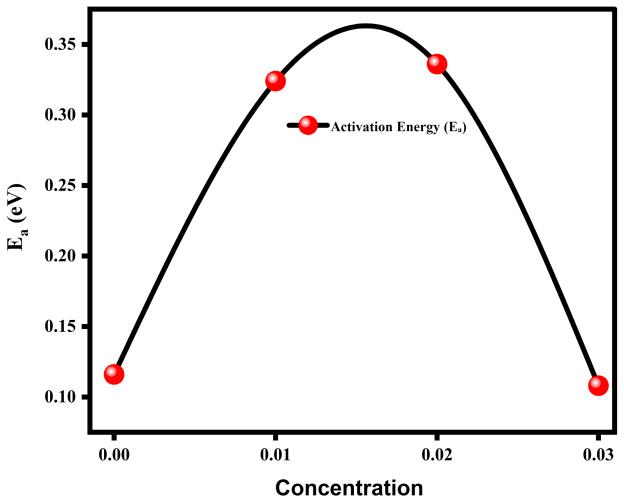


Fig. 8. Plot of Ca^{2+} concentrations versus Activation Energy (E_a) of $Zn_{0.25}Co_{0.5}Ca_{0.25}Fe_{1.97}Ba_{0.03-y}Ca_yO_4$.

3.5 Dielectric Analysis

The dielectric properties of ferrite-based materials are essential to their performance in applications such as sensors, microwave absorption, electromagnetic devices, and spintronic components. These properties are strongly influenced by the polarization processes, the charge-carrier type, and the material's microstructural features, such as grain size and grain-boundary dispersion [20,30]. Specifically, changing the cations in spinel ferrites can drastically change the frequency response, electrical resistivity, and dielectric constant, providing a structure that can be adjusted to optimize useful characteristics [31].

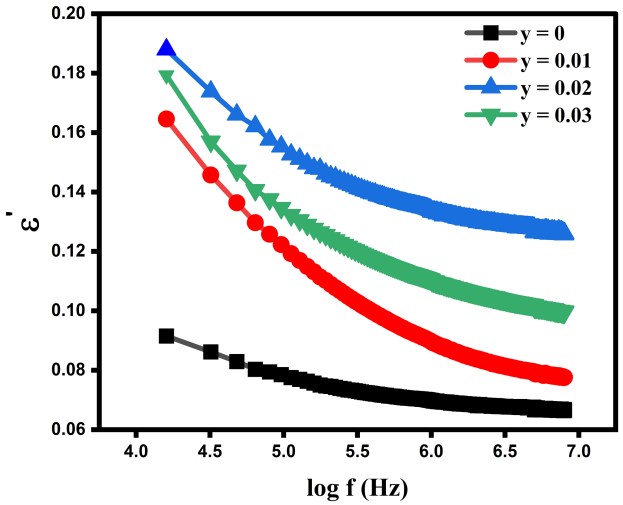


Fig. 9. Log of frequency versus real part of permittivity of $Zn_{0.25}Co_{0.5}Ca_{0.25}Fe_{1.97}Ba_{0.03-y}Ca_yO_4$.

The frequency-dependent real part of permittivity (ε′) is depicted in Fig. 9. The real permittivity (ε′) decreases monotonically with frequency for all compositions, consistent with Maxwell–Wagner interfacial polarization at grain boundaries [32,33]. Ca^{2+} substitution systematically enhances ε′ due to increased oxygen vacancies and grain boundary defect states serving as additional polarization centers. The y = 0.02 composition exhibits the highest ε′ across the full frequency range, with a plateau above 10^5 Hz indicating that its dielectric relaxation frequency lies within the MHz range, consistent with the targeted EMI shielding application. The persistent separation of all curves confirms the contribution of faster ionic and electronic polarization mechanisms, in addition to slow space-charge effects. The frequency dependency of the imaginary component of the permittivity (ε″) as presented in Fig. 10 is further supports the Maxwell–Wagner interfacial polarization mechanism [32]. The absence of a Debye relaxation peak in the measured frequency range (4 Hz–8 MHz) for all compositions suggests that the characteristic relaxation frequency is below 10^4 Hz [34]. These improvements in ε″ with increasing y are believed to be caused by space charge accumulating at grain boundaries due to the increased structural disorder and oxygen vacancy concentration associated with Ca^{2+}–Ba^{2+} substitution.

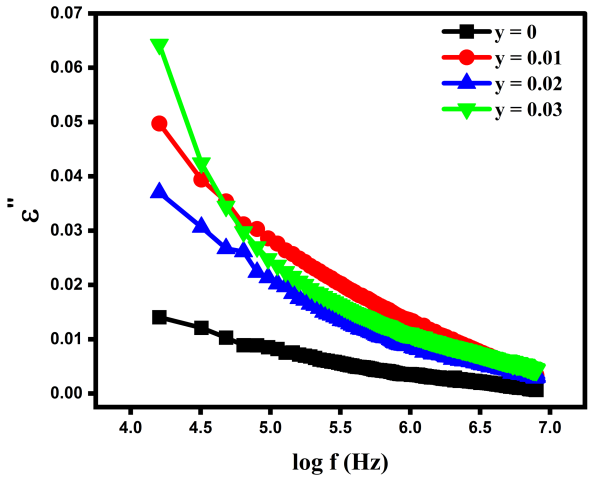


Fig. 10. Log of frequency versus imaginary part of permittivity of $Zn_{0.25}Co_{0.5}Ca_{0.25}Fe_{1.97}Ba_{0.03-y}Ca_yO_4$.

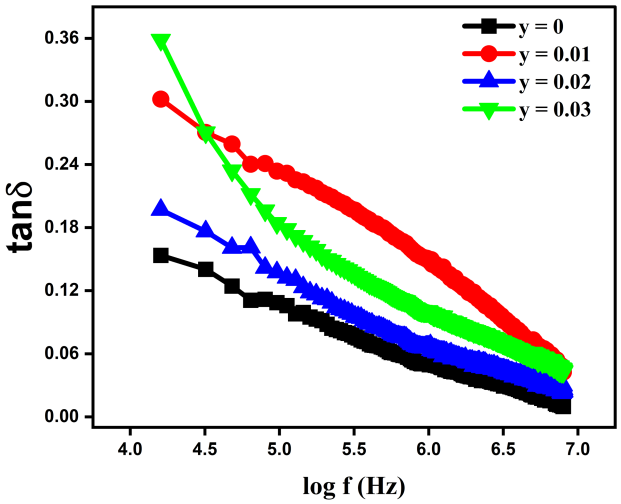


Fig. 11. Log of frequency versus dielectric tangent loss of $Zn_{0.25}Co_{0.5}Ca_{0.25}Fe_{1.97}Ba_{0.03-y}Ca_yO_4$.

The frequency dependence of the dielectric loss tangent (tanδ) for all the $Zn_{0.25}Co_{0.5}Ca_{0.25}Fe_{1.97}Ba_{0.03-y}$ compositions is presented in Fig. 11. All samples show the monotonic decrease of tan δ with increasing frequency, which is consistent with Koop's phenomenological model, where highly resistive grain boundaries dominate the response at low frequencies and conducting grains control the behavior at high frequencies [35]. The tan δ value is maximum for the y = 0.03 composition at low frequency, which is due to the increase in oxygen vacancies and an increase in interfacial polarization due to excess Ca^{2+} substitution in

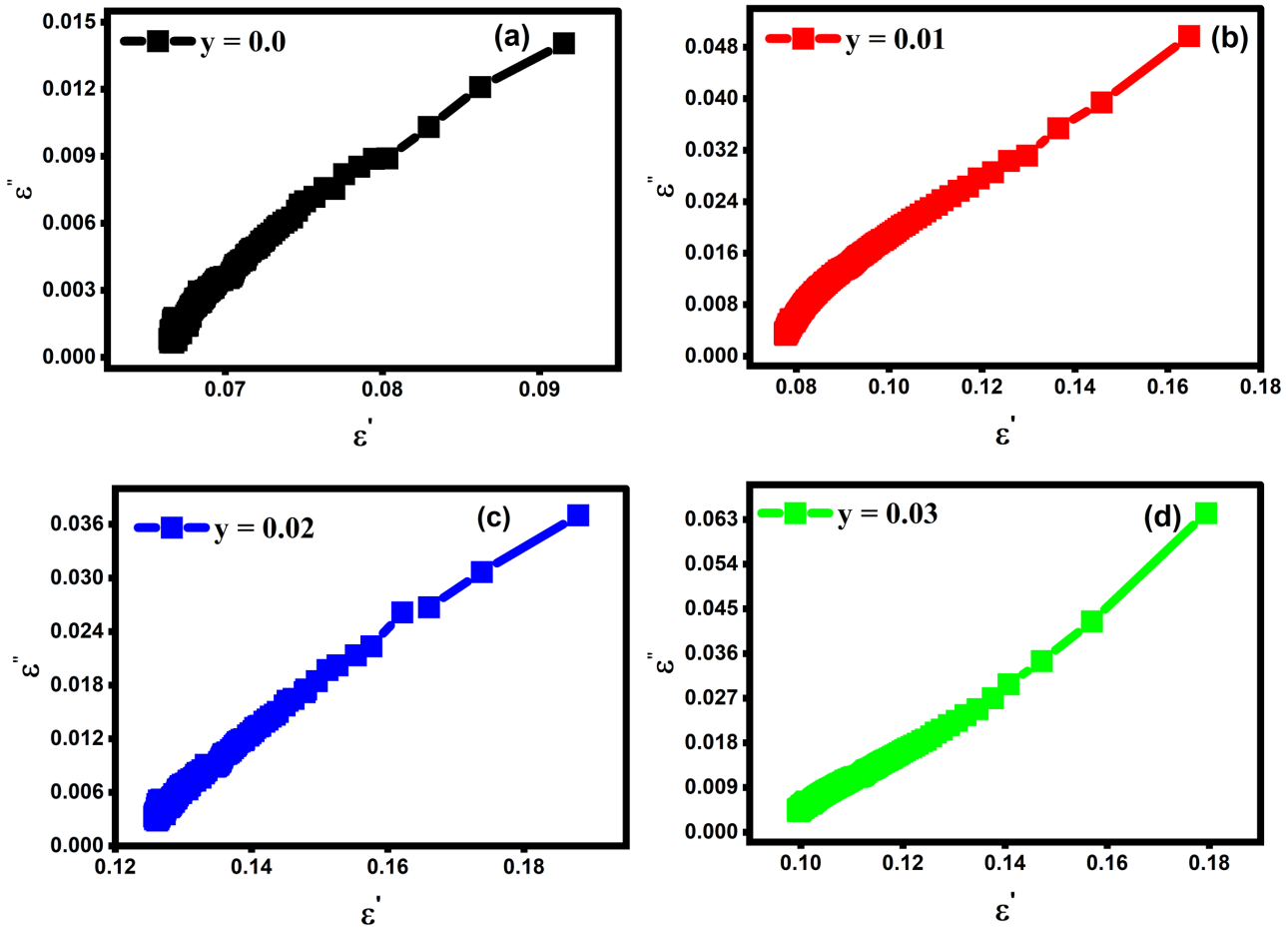


Fig. 12. Cole–Cole plots of $Zn_{0.25}Co_{0.5}Ca_{0.25}Fe_{1.97}Ba_{0.03-y}Ca_yO_4$ for different values of y. (a) y = 0.00, (b) y = 0.01, (c) y = 0.02, and (d) y = 0.03.

the composition. The non-monotonic ordering (y = 0.01 > y = 0.02) is due to opposing effects of cation redistribution and grain boundary scattering, and the maximum hopping conductivity is found at y = 0.01. It is noteworthy that all compositions converge to low tan δ values (~0.02–0.06) at 10^7 Hz, which indicate low dielectric loss in the MHz operational range pertinent to biomedical EMI shielding applications.

The Cole-Cole plots (ε″ vs ε′) for all compositions, shown in Fig. 12a–d, exhibit skewed arcs without semicircular closure, confirming non-Debye dielectric relaxation with a distribution of relaxation times arising from grain boundary heterogeneity [36]. The arc gradually moves towards higher values of ε′ as the Ca^{2+} content increases, which is consistent with increased real permittivity resulting from added polarization centers. The y = 0.03 composition shows the highest ε″ and the most linear arc trajectory, which corresponds to the maximum structural disorder at excess Ca^{2+} concentration, resulting in a broad relaxation time distribution. The composition for y = 0.02 exhibits the widest ε′ range with moderate ε″.

The frequency dependence behavior of impedance (Z) for $Zn_{0.25}Co_{0.5}Ca_{0.25}Fe_{1.97}Ba_{0.03-y}Ca_yO_4$ samples measured over the frequency range of 4 Hz to 8 MHz is shown in Fig. 13. A decreasing trend in impedance with increasing frequency was observed, a typical ferrite behavior. This trend is attributed to space charge polarization at low frequencies, where electrical transport is dominated by interfacial effects and grain boundary contributions [36]. All of the curves converge at higher frequencies, suggesting bulk-dominated conduction. These findings demonstrate that the material's electrical transport characteristics are greatly impacted by calcium substitution, making it flexible for high-frequency applications.

Fig. 14 shows the variation of alternating current (AC) conductance (G) with logarithmic of frequency. All samples exhibit an increase in conductance with frequency, a common trend for ferrites and dielectric materials because higher frequencies promote hopping mechanisms. The sample with calcium concentration y = 0.01, shows high conductance, suggesting enhanced hopping between localized states or better charge carrier mobility. Conductance decreases with substitutions y = 0.02, y = 0.03 which is

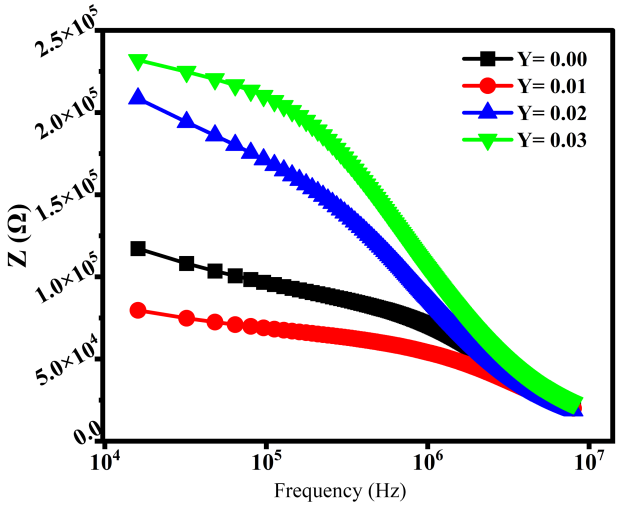


Fig. 13. Frequency versus impedance of $Zn_{0.25}Co_{0.5}Ca_{0.25}Fe_{1.97}Ba_{0.03-y}Ca_yO_4$.

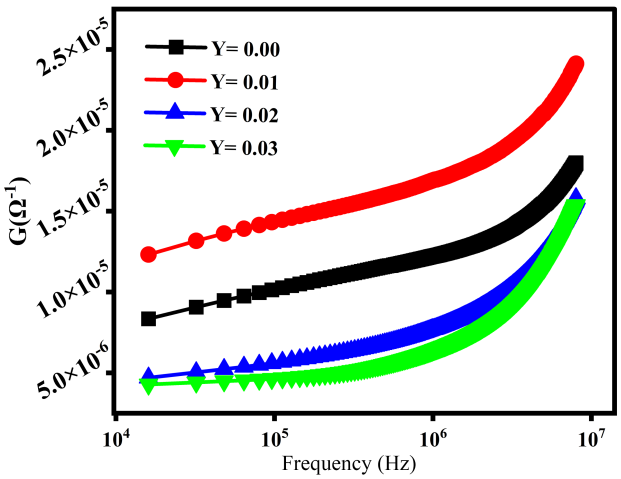


Fig. 14. Log of frequency versus AC (alternating current) conductance of $Zn_{0.25}Co_{0.5}Ca_{0.25}Fe_{1.97}Ba_{0.03-y}Ca_yO_4$.

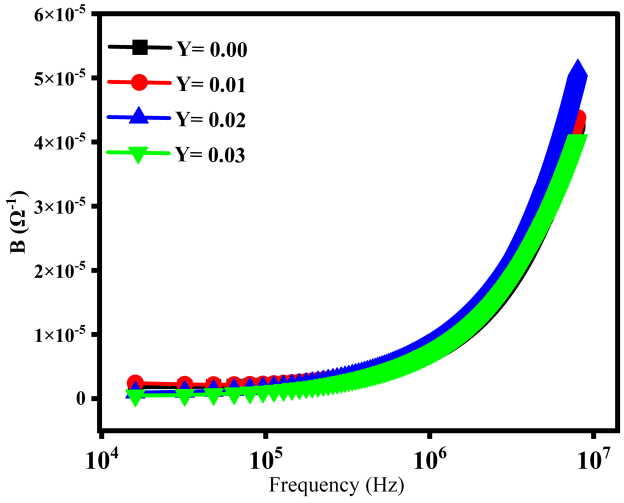


Fig. 15. Logarithm of frequency versus susceptance of $Zn_{0.25}Co_{0.5}Ca_{0.25}Fe_{1.97}Ba_{0.03-y}Ca_yO_4$.

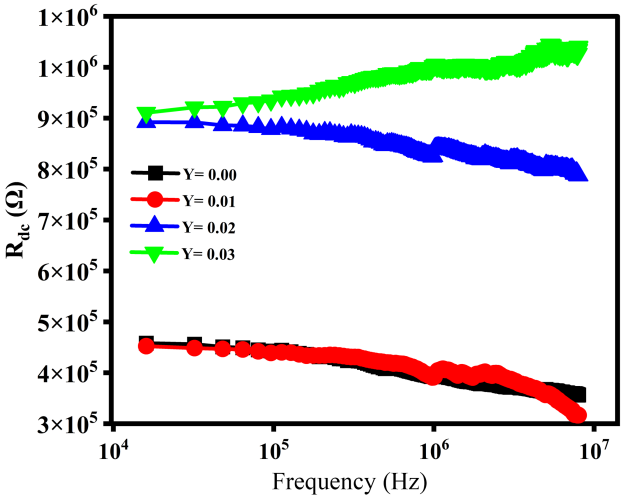


Fig. 16. Logarithm of frequency versus DC (direct current) resistance of $Zn_{0.25}Co_{0.5}Ca_{0.25}Fe_{1.97}Ba_{0.03-y}Ca_yO_4$.

due to increased lattice distortion and defect concentration [37]. The observed frequency-dependent behavior of AC conductance can be explained using Koop's theory, which models ferrites as composed of highly conductive grains separated by poorly conductive grain boundaries. At low frequencies, grain boundary resistance dominates, resulting in lower conductance, whereas at higher frequencies, the contribution from grains increases, leading to enhanced hopping conduction. These findings suggest that calcium substitution has a substantial impact on the material's conduction behavior, with y = 0.01 being the optimal composition for improved AC conductivity.

Fig. 15 represents the frequency-dependent behavior of the susceptance (B) of the as-prepared samples. All samples exhibit relatively low and nearly constant susceptance at lower frequencies (<10^5 Hz), indicating a limited contribution of capacitive conduction in this frequency range. B increases sharply with frequency, indicating an enhanced capacitive response and dielectric polarization at higher frequencies. Although there are only minor variations across the compositions, the y = 0.02 and y = 0.03 samples show somewhat greater susceptance at high frequencies, indicating improved dielectric polarization. Calcium replacement has a more noticeable effect on bulk capacitive dynamics at higher frequencies, but it has no discernible effect on interfacial polarization, according to the convergence of all curves at low frequencies.

Fig. 16 shows the graph of DC resistance and the log of frequency for prepared samples. T The DC resistance decreases slightly at y = 0.01 (lowest among all samples) and then increases significantly for y = 0.02 and 0.03. This shows that the moderate Ca^{2+} doping increases the electrical conductivity. This implies that the lattice becomes dis-

ordered due to excessive doping. Both the optimally doped sample (y = 0.01) and the undoped sample (y = 0) exhibit very low resistance, demonstrating that increased doping breaks the conductive network, whereas balanced substitution enhances electrical performance.

4. Discussions

The observed lattice distortion and phonon mode evolution induced by Ca^{2+} substitution play a crucial role in enhancing magneto-dielectric loss mechanisms, thereby improving electromagnetic wave attenuation in EMI shielding applications relevant to biomedical electronic systems.

The optimized magnetic parameters observed for the y = 0.02 composition, including high saturation magnetization, coercivity, and anisotropy constant, are particularly favorable for EMI shielding applications, as they promote magnetic loss and resonance-based absorption in the MHz frequency range. Such characteristics are essential for suppressing electromagnetic interference in biomedical diagnostic and monitoring devices.

Improved electronic structure and grain connection reduce the energy barrier and increase conductivity at higher Ca levels. The drop in E_a at y = 0.03 referred to the existence of more effective hopping mechanisms. These findings provide an ideal doping range for adjusting electrical characteristics and confirming the semiconducting behavior.

The semiconducting nature and tunable activation energy of the synthesized ferrites contribute to resistive loss mechanisms, thereby converting incident electromagnetic energy into thermal dissipation. This behavior supports their potential application as EMI shielding materials in biomedical electronic environments.

It is important to note that the EMI shielding performance of the synthesized ferrites has not been directly measured in this study. The proposed suitability for EMI shielding applications is inferred from the observed magnetic loss, dielectric polarization, and semiconducting behavior, which are known to contribute to electromagnetic wave attenuation in the MHz frequency range.

Limitation

There are several limitations to this research that should be addressed. First, microstructure characterization methods such as Scanning Electron Microscopy (SEM) or Transmission Electrn Microscopy (TEM) were not performed, so the morphology of nanoparticles and their grain size distribution were not directly observed but were only indirectly inferred from the broadening of XRD peaks. Second, elemental analysis techniques like Energy-Dispersive X-ray Spectroscopy (EDS) or elemental mapping were not performed, and, as a result, Ca^{2+} ion incorporation into the host lattice was not directly verified. Third, despite the suggestion that these materials can be used as EMI shielding materials, no direct measurement of Shielding Effectiveness (SE), reflection losses, and absorption performance was done. As a consequence, the conclusion about EMI shielding is drawn based only on indirect correlation with magnetic, dielectric, and electrical parameters. In addition, advanced structure characterization techniques like Mössbauer spectroscopy, and X-ray Photoelectron Spectroscopy (XPS) were not applied to verify the cation distribution. In future studies, researchers will strive to overcome these shortcomings.

5. Conclusion

The present study confirms that the controlled substitution of Ba^{2+} with Ca^{2+} on Zn-Co-Ca spinel ferrites enables the precise tuning of magnetic, electrical, and dielectric properties. Spinel structure is confirmed by XRD analysis. Raman spectroscopy revealed lattice distortions and phonon mode evolution, indicating enhanced structural disorder with higher Ca^{2+} concentration. Soft ferromagnetic behavior was confirmed across all samples by VSM analysis, revealing that the sample with calcium concentration y = 0.02 shows the highest M_s value (72.73 emu/g), M_r (33.97 emu/g), and H_c (746.92 Oe). Semiconducting behavior was confirmed by I-V analysis, which showed that the activation energy peaks at y = 0.02. Dielectric analysis showed that the sample y = 0.01 had the highest conductance and lowest DC resistance. The optimized compositions exhibit enhanced magnetic loss, semiconducting behavior, and frequency-dependent dielectric response, which are critical parameters for effective electromagnetic attenuation. The frequency-dependent impedance, conductance, and susceptance behavior demonstrate the combined contribution of interfacial polarization, hopping conduction, and dielectric loss mechanisms. Considering both magnetic and dielectric contributions, y = 0.02 is more suitable for EMI shielding due to strong magnetic loss.

Availability of Data and Materials

The datasets generated or analyzed during the current study are not publicly available due to research constraints, but are available from the corresponding author on reasonable request.

Author Contributions

MIA, MA, NA, and UM conceived and designed the study. MIA, MA, ZM, and KM performed the experimental work, including synthesis of nanocomposites and measurements. ABAEN, HTA, and MAuN contributed to the analysis and interpretation of structural, magnetic, dielectric, and optical data. MAuN, NA, and UM drafted the manuscript. All authors have participated sufficiently in the work and agree to be accountable for all aspects of the work.

Ethics Approval and Consent to Participate

Not applicable.

Acknowledgment

The authors would like to acknowledge the Deanship of Graduate Studies and Scientific Research, Taif University for funding this work.

Funding

This work received financial support from the Deanship of Graduate Studies and Scientific Research, Taif University.

Conflicts of Interest

The authors declare no conflicts of interest.

References

[1] Lin Q, Xu J, Yang F, Lin J, Yang H, He Y. Magnetic and Mössbauer Spectroscopy Studies of Zinc-Substituted Cobalt Ferrites Prepared by the Sol-Gel Method. Materials. 2018; 11: 1799. https://doi.org/10.3390/ma11101799

[2] Hossain MS, Alam MB, Shahjahan M, Begum MHA, Hossain MM, Islam S, et al. Synthesis, structural investigation, dielectric and magnetic properties of Zn2+-doped cobalt ferrite by the sol–gel technique. Journal of Advanced Dielectrics. 2018; 8: 1850030. https://doi.org/10.1142/s2010135x18500303

[3] El-Shater R, Sad NIA, Abdel-Khalek EK, Meaz TM, El-Nimr MK, Fakhry F, et al. Syenthis, structural, magnetic, optical, and dielectric properties of ag and cr substituted Co-ferrite nanoparticles. Scientific Reports. 2025; 15: 38493. https://doi.org/10.1038/s41598-025-22606-x

[4] Ramesh KV, Venkatesh D. Effect of copper substitution on structural, electrical, and magnetic properties of nanocrystalline cobalt ferrites for memory storage applications. physica status solidi (b). 2025; 262: 2400453. https://doi.org/10.1002/pssb.202400453

[5] Thakur A, Verma R, Wan F, Ravelo B, Edelman I, Ovchinnikov S, et al. Investigation of structural, elastic and magnetic properties of Cu^{2+} ions substituted cobalt nano ferrites. Journal of Magnetism and Magnetic Materials. 2023; 581. https://doi.org/10.1016/j.jmmm.2023.170980

[6] Jain P, Shankar S, Thakur OP. Unveiling the impact of Ni^{2+}/Y^{3+} co-substitution on the structural, dielectric, and impedance properties of multiferroic spinel ferrite for hydroelectric cell application. Physical Chemistry Chemical Physics. 2023; 25: 21280–21296. https://doi.org/10.1039/d3cp02339g

[7] Farzana Alam M, Atikur Rahman M, Hossain MS, Khan MNI, Rashid R, Saiful Islam M, et al. Synthesis and magneto-dielectric properties of Ti-doped $Ni_{0.5}$ $Zn_{0.5}$ Ti_x Fe_{2-x} O_4 ferrite *via* a conventional sol–gel process. Materials Advances. 2024; 5: 9041–9054. https://doi.org/10.1039/d4ma00529e

[8] Jain P, Shankar S, Thakur O. Unveiling the structural, optical, electrical, and ferromagnetic properties of Ca2+ doped mixed spinel ferrites for switching field high-frequency device applications. Ceramics International. 2024; 50: 48354–48372. https://doi.org/10.1016/j.ceramint.2024.09.185

[9] Khoreem SH, AL-Hammadi AH. Effect of Nonmagnetic Doping on Dielectric Properties and Initial Permeability of Ba-Ni Ferrite Nanoparticles by Virtue of Zn^{2+} Ions. Advances in Materials Science and Engineering. 2023; 2023: 5586664. https://doi.org/10.1155/2023/5586664

[10] Mahadevan S, Sharma P. Charge transport mechanism in $BaFe_{12}O_{19}$ and $BaFe_{11}CoO_{19}$. Journal of Magnetism and Magnetic Materials. 2020; 514: 167174. https://doi.org/10.1016/j.jmmm.2020.167174

[11] Nazir S, Zhang JM, Qadir K, Saleem S. Investigation of Structural, Morphological and Optical Properties of Ni-Doped $ZnFe_2O_4$ Nanoparticles Synthesized by Sol-Gel Auto-Combustion Method. Physics of Metals and Metallography. 2024; 125: S13–S20. https://doi.org/10.1134/S0031918X24601033

[12] Lu H, Li C, Chen K, He Q, Ren F, Wu J, et al. Facile synthesis of $CoFe_2O_4$@SiO_2 nanoparticles anchored on reduced graphene oxide for highly efficient electromagnetic wave absorption. RSC Advances. 2025; 15: 25872–25884. https://doi.org/10.1039/d5ra03579a

[13] Zahran AI, El-Fawal EM, Naggar AMAE, Hassanein TF. Production of low sulfur diesel fuel through ultrasonic catalytic oxidative route using novel mixed oxides nanocomposites assisted by solvent extraction. Scientific Reports. 2026; 16: 12058. https://doi.org/10.1038/s41598-026-39220-0

[14] Sen SK, Barman UC, Manir MS, Mondal P, Dutta S, Paul M, et al. X-ray peak profile analysis of pure and Dy-doped α-MoO_3 nanobelts using Debye-Scherrer, Williamson-Hall and Halder-Wagner methods. Advances in Natural Sciences: Nanoscience and Nanotechnology. 2020; 11: 025004. https://doi.org/10.1088/2043-6254/ab8732

[15] Shebanova ON, Lazor P. Raman study of magnetite (Fe_3O_4): laser-induced thermal effects and oxidation. Journal of Raman Spectroscopy. 2003; 34: 845–852. https://doi.org/10.1002/jrs.1056

[16] Mrabet S, Ihzaz N, Bessadok MN, Vázquez-Vázquez C, Alshammari M, El Mir L. Microstructural, Raman, and Magnetic Investigations on Ca-doped ZnO Nanoparticles. Journal of Inorganic and Organometallic Polymers and Materials. 2024; 34: 2064–2073. https://doi.org/10.1007/s10904-023-02947-8

[17] Kim K, Park J, Park JY. Co^{2+} Distribution and the Related Magnetic Evolution in Ca-substituted Spinel $CoFe_2O_4$. Journal of Magnetics. 2021; 26: 410–414. https://doi.org/10.4283/jmag.2021.26.4.410 (In Korean)

[18] Albini B, Restelli S, Ambrosetti M, Bini M, D'Amico F, Mozzati MC, et al. Raman spectroscopy in pure and doped zinc ferrites nanoparticles. Journal of Materials Science: Materials in Electronics. 2023; 34. https://doi.org/10.1007/s10854-023-10464-0

[19] Kumar R, Kar M. Correlation between lattice strain and magnetic behavior in non-magnetic Ca substituted nano-crystalline cobalt ferrite. Ceramics International. 2016; 42: 6640–6647. https://doi.org/10.1016/j.ceramint.2016.01.007

[20] Amiri M, Salavati-Niasari M, Akbari A. Magnetic nanocarriers: Evolution of spinel ferrites for medical applications. Advances in Colloid and Interface Science. 2019; 265: 29–44. https://doi.org/10.1016/j.cis.2019.01.003

[21] Egli R, Lowrie W. Anhysteretic remanent magnetization of fine magnetic particles. Journal of Geophysical Research: Solid Earth. 2002; 107: EPM 2. https://doi.org/10.1029/2001jb000671

[22] Gabal M, Al Angari Y, Al-Agel F. Synthesis, characterization and magnetic properties of Cr-substituted Co–Zn ferrites nanopowders. Journal of Molecular Structure. 2013; 1035: 341–347. https://doi.org/10.1016/j.molstruc.2012.10.061

[23] Niu ZP, Wang Y, Li FS. Magnetic properties of nanocrystalline Co–Ni ferrite. Journal of Materials Science. 2006; 41: 5726–5730. https://doi.org/10.1007/s10853-006-0099-3

[24] Katoch G, Himanshi, Jasrotia R, Prakash J, Verma A, Kandwal A, et al. Crystal structure, synthesis, properties and potential applications of cobalt spinel ferrite: A brief review. Materials Today: Proceedings. 2023. https://doi.org/10.1016/j.matpr.2023.03.585

[25] Houbi A, Aldashevich ZA, Atassi Y, Telmanovna ZB, Saule M, Kubanych K. Microwave absorbing properties of ferrites and their composites: A review. Journal of Magnetism and Magnetic

Materials. 2021; 529: 167839. https://doi.org/10.1016/j.jmmm.2021.167839
[26] Sheikh AD, Mathe VL. Anomalous electrical properties of nanocrystalline Ni–Zn ferrite. Journal of Materials Science. 2008; 43: 2018–2025. https://doi.org/10.1007/s10853-007-2302-6
[27] Jalaiah K, Mouli KC, Krishnaiah RV, Babu KV, Rao PSVS. The structural, DC resistivity and magnetic properties of Zr and Co co-substituted $Ni_{0.5}Zn_{0.5}Fe_2O_4$. Heliyon. 2019; 5: e01800. https://doi.org/10.1016/j.heliyon.2019.e01800
[28] Assar S, El-Ghazzawy E, Abosheiasha H. Study on dielectric properties, electric modulus, and impedance spectroscopy of Ni–Ca ferrite nanoparticles. Materials Chemistry and Physics. 2022; 287: 126336. https://doi.org/10.1016/j.matchemphys.2022.126336
[29] Dionne G. A review of ferrites for microwave applications. Proceedings of the IEEE. 1975; 63: 777–789. https://doi.org/10.1109/proc.1975.9827
[30] Pullar RC. Hexagonal ferrites: A review of the synthesis, properties and applications of hexaferrite ceramics. Progress in Materials Science. 2012; 57: 1191–1334. https://doi.org/10.1016/j.pmatsci.2012.04.001
[31] Ikram S, Jacob J, Mehboob K, Mahmood K, Amin N, Arshad MI, et al. Role of Rare Earth Metal Ions Doping on Structural, Electrical, Magnetic, and Dielectric Behavior of Spinel Ferrites: a Comparative Study. Journal of Superconductivity and Novel Magnetism. 2021; 34: 1833–1842. https://doi.org/10.1007/s10948-020-05688-8
[32] Yue D, Geng T, Liu J, Qi J, Wang Y, Kong W, et al. Research of Radiation Tolerance via Polyimide Matrix Multilayer Dielectric Structures. IEEE Transactions on Dielectrics and Electrical Insulation. 2026; 1–1. https://doi.org/10.1109/tdei.2026.3690143
[33] Munir Z, Arshad MI, Amin N, Iqra, Akhtar M, Al-Buriahi M, et al. Optimized EMI shielding effectiveness of Co-Cu-Gd spinel ferrites reinforced with graphene nanoplatelets. Ceramics International. 2026; 52: 29338–29348. https://doi.org/10.1016/j.ceramint.2026.05.013
[34] Iqra, Arshad MI, Munir Z, Amin N, Akhtar M, Al-Buriahi M, et al. Enhanced absorption-dominant EMI shielding effectiveness by multi-dimensional $Mg_{0.33}Ca_{0.33}Cu_{0.34}Fe_2O_4/GO$ nanocomposites under applied magnetic fields. Ceramics International. 2026; 52: 23433–23446. https://doi.org/10.1016/j.ceramint.2026.03.395
[35] Kossi SE, Rayssi C, Dhahri AH, Dhahri J, Khirouni K. High dielectric constant and relaxor behavior in $La_{0.7}Sr_{0.25}Na_{0.05}Mn_{0.8}Ti_{0.2}O_3$ manganite. Journal of Alloys and Compounds. 2018; 767: 456–463. https://doi.org/10.1016/j.jallcom.2018.07.056
[36] Munir Z, Amin N, Arshad MI. Magneto-dielectric properties of GNPs modified $Co_{0.7}Cu_{0.3}Ho_{0.1}Fe_{1.9}O_4$ nanocomposites with the balanced dielectric-magnetic loss for high frequency applications. Ceramics International. 2025; 51: 34440–34454. https://doi.org/10.1016/j.ceramint.2025.05.169
[37] Na J, Lee T, Park S. Effects of cation distribution on the magnetic and electrical properties of cobalt ferrite. IEEE Transactions on Magnetics. 1992; 28: 2433–2435. https://doi.org/10.1109/20.179516